

Spectroscopic and Computational Interrogation of a High-Valent Nickel-Dialkyl Complex Indicates Electronic Structure Asymmetry Drives C–C Bond Formation Reactivity

Alina Yerbulekova,[#] Yusuff Moshood,[#] Leonel Griego, Hannah S. Shafaat,^{*} and Liviu M. Mirica^{*}



Cite This: *J. Am. Chem. Soc.* 2025, 147, 7317–7324



Read Online

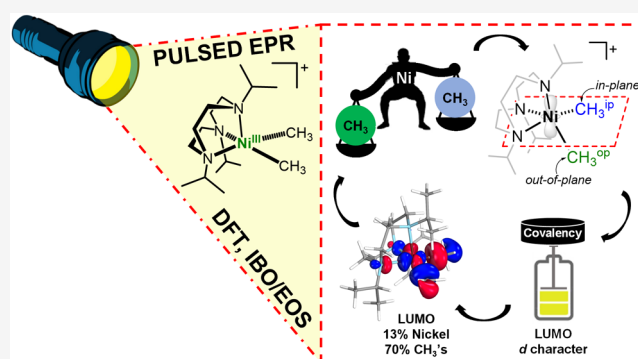
ACCESS |

Metrics & More

Article Recommendations

Supporting Information

ABSTRACT: The study of high-valent organometallic nickel compounds has gained considerable interest recently, primarily driven by the development of nickel-catalyzed alkyl–alkyl cross-coupling reactions that are proposed to employ such high-valent intermediates. In that regard, we have recently reported a formal Ni(III)-dimethyl intermediate supported by the ligand *N,N,N'*-triisopropyl-1,4,7-triazacyclononane (*i*Pr₃tacn) that can undergo rapid C–C reductive elimination and catalyze alkyl–alkyl Kumada cross-coupling reactions. The bulky nature of this tridentate ligand was suggested to lead to two geometrically and electronically inequivalent alkyl groups bound to the five-coordinate Ni center. Herein, we have employed pulsed electron paramagnetic resonance techniques such as electron nuclear double resonance, hyperfine sublevel correlation, and electron spin echo envelope modulation to provide strong experimental evidence for the geometrically and electronically inequivalent nature of the two methyl groups in which one methyl ligand can be better described as a methyl radical. These experimental results were supported by density functional theory computational methods used to probe the covalent nature of the Ni–C bonds and the formal Ni oxidation state assignment for this catalytically relevant, high-valent Ni intermediate. Moreover, computational investigation of a series of related methyl/alkyl analogs reveals that the radical character of an alkyl group increases for a tertiary vs a secondary vs a primary alkyl group, with direct relevance for alkyl–alkyl cross-coupling catalysis. Overall, this study provides valuable insights into the nature of organometallic Ni-dialkyl species that undergo efficient reductive elimination, likely through an S_H2-type mechanism.



INTRODUCTION

Recently, there has been significant interest in nickel-catalyzed cross-coupling reactions, primarily due to their ability to promote alkyl–alkyl coupling reactions, including stereoselective transformations.^{1–5} In contrast to palladium-catalyzed cross-coupling reactions that commonly employ a Pd(0)/Pd(II) catalytic cycle, numerous studies have provided evidence for the participation of Ni^I and Ni^{III} organometallic intermediates in Ni-catalyzed cross-coupling reactions, which commonly employ radical species and single electron transfer processes.^{5–11} In these organometallic Ni systems, it is widely accepted that both the metal oxidation state and the ligand's electronic and steric properties play a crucial role in determining the electron distribution between the ligand and the metal, which ultimately modulates the reactivity of the highly covalent metal–alkyl/aryl bonds. Consequently, an increase in valency and the presence of geometric constraints have been proposed to create an unusual ligand field environment.¹² In this regard, several studies have focused on understanding the metal center oxidation state assignment and bonding interactions involving high-valent complexes of

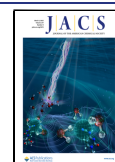
low symmetry. Using computational methods, Klein et al. probed a formal Ni^{IV} organometallic center¹³ and revealed the role of ligand σ -noninnocence on oxidation assignment (Figure 1).¹⁴ A ligand-centered LUMO was observed and a case for ligand field inversion was presented, with the Ni^{IV} center being better described as Ni^{II} due to highly covalent metal–ligand bonds. This oxidation state reassignment has mechanistic consequences for the reductive elimination step that is proposed to occur at a redox-neutral metal center. Recently, Holland et al. provided mechanistic insight into the catalytic hydrofunctionalization of alkenes via a metal hydrogen atom transfer step that involves a Co^{IV}-alkyl intermediate.¹⁵ By using electron nuclear double resonance (ENDOR) spectroscopy and density functional theory (DFT) methods, the authors

Received: October 11, 2024

Revised: February 7, 2025

Accepted: February 10, 2025

Published: February 24, 2025



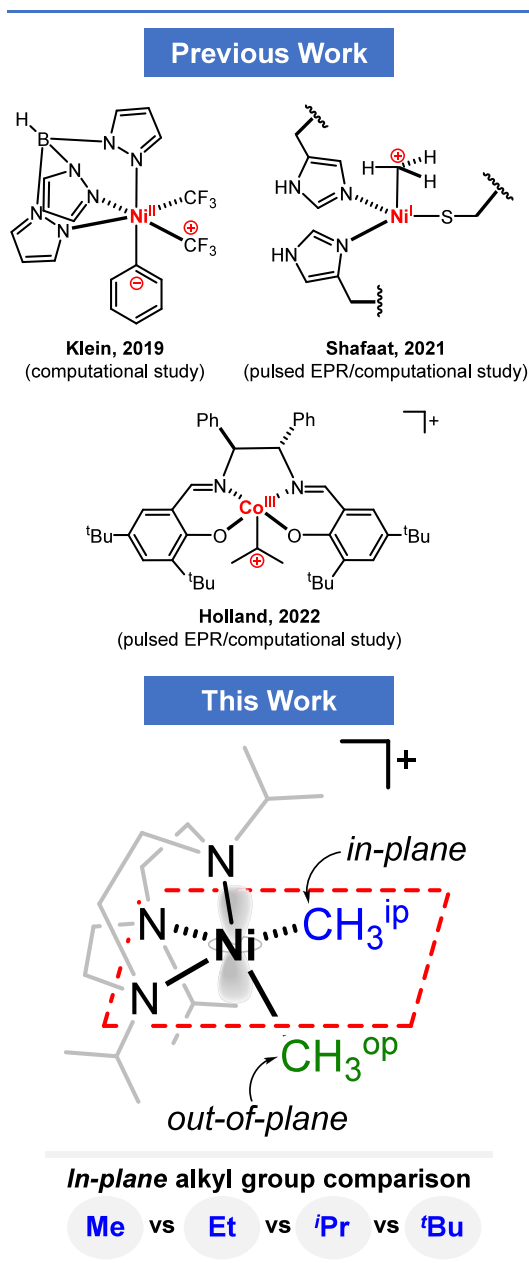


Figure 1. Reported organometallic high-valent transition metal complexes that exhibit an inverted ligand field (top) and the $[(\text{Pr}_3\text{TACN})\text{Ni}(\text{CH}_3)_2]^+$ complex 3 investigated herein, along with the related computationally probed methyl/alkyl analogs (bottom).

provided evidence for the formation of a high-valent cobalt–isopropyl σ -bond, and natural bonding orbital (NBO) analysis suggested the presence of an inverted ligand field, in which the

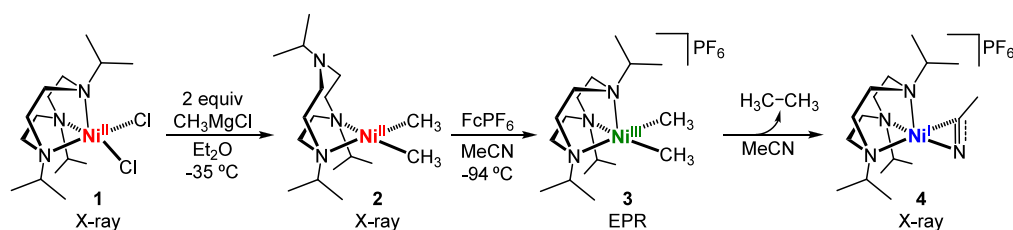
formal Co^{IV} species can be viewed as Co^{II} interacting with a cationic isopropyl group (Figure 1).

In 2021, Shafaat et al. studied extensively the electronic structure of a formal Ni^{III} biomimetic model of acetyl coenzyme A synthase (ACS) in the context of its reactivity (Figure 1),¹⁶ and an inverted ligand field was also invoked in this system. Detailed pulsed EPR data clearly support the idea that the methyl group undergoes a structural distortion from tetrahedral to almost planar, suggestive of a cationic methyl group (or a methyl radical). Starting in 2019, Lancaster et al. have employed detailed metal K-edge and $L_{2,3}$ -edge X-ray absorption spectroscopy (XAS) and computational studies to probe high-valent copper and nickel complexes with significantly covalent metal–ligand bonds, and have clearly shown that such systems adopt an inverted ligand field that has direct implications in metal oxidation state assignment and their redox reactivity.^{17–20}

Spectroscopic evidence for a Ni^{III} -dialkyl organometallic species relevant to cross-coupling reactions has been previously reported by our group.^{21–25} In one recent case, we have just reported a Ni^{III} -dimethyl intermediate supported by the ligand N,N',N'' -triisopropyl-1,4,7-triazacyclononane (Pr_3TACN) that can undergo rapid C–C reductive elimination and catalyze alkyl–alkyl Kumada cross-coupling reactions (Scheme 1).²⁶ While in the square-planar $(\text{Pr}_3\text{TACN})\text{Ni}^{\text{II}}(\text{CH}_3)_2$ complex 2 the two methyl groups are equivalent, in the five-coordinate $(\text{Pr}_3\text{TACN})\text{Ni}^{\text{II}}\text{Cl}_2$ complex 1 the bulky nature of the Pr_3TACN ligand imposes a geometric restriction that renders the chlorides inequivalent.^{27,28} The X-band EPR characterization of complex 3 reveals that the axial nitrogen interacts with the Ni^{III} center and thus suggests a five-coordinate geometry, thus raising the possibility that the two methyl groups are geometrically and electronically inequivalent. Since Ni^{III} -dimethyl species 3 is highly reactive and undergoes reductive elimination even at lower temperatures, it could not be structurally characterized.

Based on this proposed distorted 5-coordinate geometry of the Ni center in complex 3, we sought to provide experimental evidence for the geometrically and electronically inequivalent nature of the two methyl groups and whether this inequivalence persists in solution. The use of pulsed electron paramagnetic resonance (EPR) techniques such as ENDOR, hyperfine sublevel correlation (HYSCORE), and electron spin echo envelope modulation (ESEEM) reveals the inequivalent nature of the two methyl groups, in which one methyl ligand can be better described as a methyl radical. DFT computational methods were then employed to investigate the covalent nature of the Ni–C bonds and the Ni oxidation state assignment for this catalytically relevant high-valent Ni intermediate. Moreover, we have extended the computational analysis to Ni-dialkyl species containing two different alkyl groups to provide evidence for the preferred localization of the

Scheme 1. Synthesis of the $[(\text{Pr}_3\text{TACN})\text{Ni}^{\text{III}}(\text{CH}_3)_2]\text{PF}_6$ Complex 3 and Its Reductive Elimination Reactivity²⁶



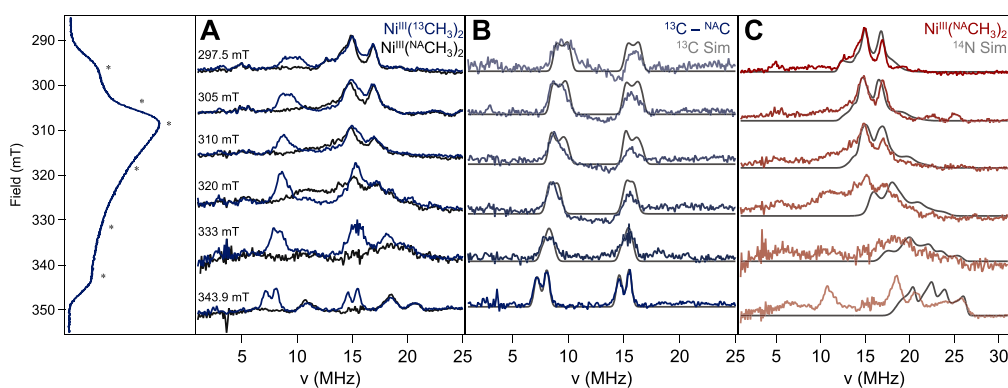


Figure 2. X-band Davies ENDOR spectroscopy on $\text{Ni}^{\text{III}}(\text{CH}_3)_2$. (A) ENDOR spectra of natural abundance (^{14}N , black) and ^{13}C -labeled (blue) $\text{Ni}^{\text{III}}(\text{CH}_3)_2$ collected at different field positions within the absorption envelope (as indicated). (B) Difference spectra showing $^{13}\text{CH}_3\text{-}^{14}\text{NCH}_3$ subtracted data (blue traces) overlaid with simulations at each field position (gray traces). (C) $\text{Ni}^{\text{III}}(^{14}\text{NCH}_3)_2$ experimental data (red traces) overlaid with ^{14}N simulations (gray). $T = 5\text{ K}$; $\nu_{\mu\text{w}} = 9.72\text{--}9.74\text{ GHz}$.

radical character on the secondary and tertiary alkyl groups, thus offering a selectivity rule for the radical sorting process needed to promote efficient alkyl–alkyl cross-coupling reactions through an $\text{S}_{\text{H}}2$ -type mechanism.

MATERIALS AND METHODS

EPR Sample Preparation. The $(^i\text{Pr}_3\text{TACN})\text{Ni}^{\text{II}}(\text{CH}_3)_2$ complex **2** and its isotopologs $(^i\text{Pr}_3\text{TACN})\text{Ni}^{\text{II}}(\text{CD}_3)_2$ and The $(^i\text{Pr}_3\text{TACN})\text{-Ni}^{\text{II}}(^{13}\text{CH}_3)_2$ were prepared as recently reported.²⁶ All EPR sample preparations were conducted in a N_2 atmosphere glovebox at $\sim\text{--}95^\circ\text{C}$. An EPR tube was charged with a solution of $(^i\text{Pr}_3\text{TACN})\text{-Ni}^{\text{II}}(\text{CH}_3)_2$ ($\sim 1\text{ mg}$, 0.003 mmol) in 0.1 mL of thawing THF. Separately, 0.3 mL of 2-methyltetrahydrofuran (2-MeTHF) was used to prepare a solution containing 1 equiv of the oxidant $[\text{Cp}_2\text{Fe}]\text{PF}_6$ (FcPF_6), and the resulting solution was cooled to $\sim\text{--}95^\circ\text{C}$, and then added to the solution of the Ni^{II} complex. The resulting solution mixture ($\sim 5\text{ mM}$ in 0.4 mL of 1:3 THF:2-MeTHF) was sealed with a septum, mixed for 5 s , frozen at liquid nitrogen temperatures, then quickly taken out of the glovebox, and placed in a transportation Dewar for longer term storage and transportation.

Pulsed EPR Techniques. X-band pulsed EPR spectra were collected at the Ohio Advanced EPR Laboratory at Miami University (Oxford, OH) using a Bruker ELEXSYS E580 instrument equipped with an EN 4118-X-MD4 pulsed ENDOR resonator, a 10 W amplifier, an Oxford Instruments continuous flow helium cryostat, and a temperature controller (ESR 900). Electron spin echo-detected (ESE) field-swept spectra were measured at 5 K using the $t_p\text{-}\tau\text{-}2t_p\text{-}\tau$ -echo pulse sequence with the length of a $\pi/2$ pulse t_p set to 10 ns ($^{13}\text{C}/^{12}\text{C}$ -labeled $\text{Ni}^{\text{III}}(\text{CH}_3)_2$) or 12 ns ($^2\text{H}/^1\text{H}$ -labeled $\text{Ni}^{\text{III}}(\text{CH}_3)_2$). The interpulse distance τ was in the range $200\text{--}400\text{ ns}$, while the shot repetition time (SRT) was $1000\text{--}3000\text{ }\mu\text{s}$. T_1 inversion recovery time traces were acquired by using the $2t_p\text{-}T\text{-}t_p\text{-}\tau\text{-}2t_p\text{-}\tau$ -echo pulse sequence. $\text{Ni}^{\text{III}}(\text{CH}_3)_2$ T_1 measurements were performed at 5 K with $t_p = 10\text{ ns}$, $T = 32\text{ }\mu\text{s}$, and SRT = 10 ms . $\text{Ni}^{\text{III}}(\text{CD}_3)_2$ T_1 measurements were done at 15 K with $t_p = 16\text{ ns}$, $T = 2\text{--}4\text{ }\mu\text{s}$, and SRT = $5\text{--}10\text{ ms}$. T_2 decay experiments for $^2\text{H}/^1\text{H}$ $\text{Ni}^{\text{III}}(\text{CH}_3)_2$ were measured at 15 K with the $t_p\text{-}\tau\text{-}2t_p\text{-}\tau$ -echo pulse sequence and the following parameters: $t_p = 16\text{ ns}$, $T = 8\text{ }\mu\text{s}$, and SRT = $500\text{ }\mu\text{s}$.

$^{13}\text{C}/^{14}\text{N}$ Davies ENDOR spectroscopy at 5 K was performed at six field positions within the EPR absorption envelope of $\text{Ni}^{\text{III}}(\text{CH}_3)_2$ using $t_{\text{inv}}\text{-}t_{\text{rf}}\text{-}T\text{-}t_p\text{-}\tau\text{-}2t_p\text{-}\tau$ -echo pulse sequence with $t_{\text{inv}} = 30\text{ ns}$ (40 ns for the high-field edge position), $t_p = 10\text{ ns}$ and radio frequency pulse $t_{\text{rf}} = 15\text{ }\mu\text{s}$. The interpulse distance τ was in the range of $210\text{--}240\text{ ns}$, $T = 1000\text{ ns}$, and SRT was set to $2000\text{ }\mu\text{s}$. A stochastic acquisition mode was applied. Three-pulse ESEEM spectra for $\text{Ni}^{\text{III}}(\text{CH}_3)_2$ and $\text{Ni}^{\text{III}}(\text{CD}_3)_2$ were collected at 15 K applying the following pulse sequence $t_p\text{-}\tau\text{-}t_p\text{-}T\text{-}t_p\text{-}\tau$ -echo with $t_p = 16\text{ ns}$ and four-step phase cycling. The interpulse distance τ values were selected to suppress the solvent protons at a given field position, using $\tau = 240\text{ ns}$ at 294 mT , τ

$= 308\text{ ns}$ at 306.5 mT , and $\tau = 476\text{ ns}$ at 346.7 mT . The time base increment was set to $dx = 16\text{ ns}$, $T = 100\text{ ns}$, SRT = $1000\text{ }\mu\text{s}$, and 500 points were collected. HYSORE data for $\text{Ni}^{\text{III}}(\text{CH}_3)_2$ and $\text{Ni}^{\text{III}}(\text{CD}_3)_2$ samples were acquired at $5\text{--}15\text{ K}$ using the $t_p\text{-}\tau\text{-}t_p\text{-}T_1\text{-}2t_p\text{-}T_2\text{-}t_p\text{-}\tau$ -echo pulse sequence with $t_p = 10\text{--}12\text{ ns}$. Solvent suppression τ values and 16-step phase cycling were applied. Data with 128×128 points were collected with the time base increments $dx = dy = 16\text{ ns}$, interpulse distances $T_1/T_2 = 100\text{ ns}$, and SRT = $1000\text{ }\mu\text{s}$.

Pulsed EPR spectra were processed and analyzed by using the EasySpin toolbox within Matlab (R2022b). Additional processing and fitting of T_1 and T_2 data was performed using Igor Pro (Wavemetrics, v9.0). T_1 and T_2 experiments were fit to biexponential functions. For the ^{13}C ENDOR simulations, ^{12}C data were subtracted from the ^{13}C ENDOR data to remove the contributions from the strongly coupled nitrogen and secondary species. Subtracted spectra were normalized, and ENDOR simulations were performed using the EasySpin core function “salt”. Separate custom functions built on salt were used for the ^{13}C and ^{14}N simulations. An ENDOR line width of 0.5 MHz was applied for the simulations. Euler angles $[\alpha, \beta, \gamma] = [14, 16, 0]^\circ$ were included in the ^{14}N ENDOR simulations, rotating the hyperfine and quadrupole tensors with respect to the g-tensor, to obtain the best fit (Figures S9 and S10). Three-pulse ESEEM time-domain traces were processed by subtracting a polynomial background, applying a hamming window, and zero-filling. Time-domain data were converted into frequency-domain data with a cross-term averaged fast Fourier transform, and the absolute values were taken for spectral presentation. HYSORE data were processed in a similar way, followed by a 2D Fourier transform. For ESEEM and HYSORE simulations, time-domain traces of $\text{Ni}^{\text{III}}(\text{CH}_3)_2$ were subtracted from the $\text{Ni}^{\text{III}}(\text{CD}_3)_2$ data before processing to emphasize contributions from the $-\text{CD}_3$ groups. ESEEM simulations were performed using the EasySpin core function “saffron”. Custom functions built on saffron were used to simulate τ - and field-dependent data. Simulations of HYSORE spectra using the ESEEM simulation parameters were used to constrain the acceptable range of values; direct fitting to the HYSORE spectra was not performed due to the high computational demand.

Computational Studies. To investigate the geometry and electronic structure of complex **3** and the methyl/alkyl analogs, density functional theory (DFT) calculations were carried out using the ORCA 4.2.1 computational chemistry package.²⁹ Geometry optimizations were performed using the using the B3LYP^{30,31} functional along with the basis sets def2-TZVP for Ni and N atoms and def2-SV(P)³² for the other atoms. The solvation effect of acetonitrile was taken into consideration using the conductor-like polarizable continuum (CPCM) model. The optimized geometries were confirmed to be at the stationary point by Hessian calculations, resulting in no imaginary frequencies. Next, single point energies and Kohn–Sham wave functions were computed at the stationary points

using the B3LYP^{30,31} functional in combination with the def2TZVPP³² basis set, and the DFT-calculated unrestricted natural orbitals (UNOs) were employed to obtain the atomic orbital composition of the frontier molecular orbitals.³³

To further analyze the nature of the nickel-ligand bonding interactions in complex **3** and its methyl/alkyl analogs, we have employed the intrinsic bond orbital (IBO) method^{34–36} and performed the effective oxidation state (EOS) analysis using the fragment-based formalism at the same level of theory.^{14,37,38} In all cases, the fragments considered were the Ni center, the in-plane methyl or alkyl group, the out-of-plane methyl group, and the ⁱPr₃TACN ligand, respectively.

RESULTS AND DISCUSSION

Given that the reactivity of complex **3** prevents crystallographic characterization, we lack unambiguous evidence regarding the potential inequivalence of the two Ni-methyl groups and the corresponding Ni–C bond lengths. To further investigate the electronic structure of this catalytically relevant species, we utilized pulsed EPR spectroscopy. Davies ENDOR spectra were acquired at six field positions within the absorption envelope of natural abundance (NA) and ¹³C-labeled complex **3** to probe strongly coupled nuclei (Figure 2). Subtraction of ^{NA}CH₃ signals from the ¹³C-labeled data set resolves two sets of peaks in the 6–18 MHz region that are split by 2* ν_{13C} (Figure 2). A well-resolved doublet of doublets observed at the high field position confirms the coordination of two distinct methyl groups to the nickel center. Global fitting of the subtracted data provides hyperfine parameters for two strongly coupled ¹³C nuclei: the first has axial symmetry and a unique axis along $g_1 = 2.38$ with $|A(^{13}C_1)| = [27, 23.5, 23.5]$ MHz ($a_{iso} = 24.7$ MHz; $T = 1.2$ MHz; $\eta = 0$), while the second is fully rhombic with $|A(^{13}C_2)| = [24.2, 27.1, 21.5]$ MHz ($a_{iso} = 24.2$ MHz, $T = 1.4$ MHz; $\eta = 1$). While the isotropic coupling is nearly identical, consistent with a similar degree of s spin delocalization onto the carbon centers, the distinct change in symmetry reveals that the two coordinated methyl groups are not equivalent. The anisotropy of the dipolar coupling indicates significant geometric distortion of ¹³C₂, which, using a three-point dipole approximation to model the distributed spin across the d_z^2 SOMO, is consistent with lying $\sim 20^\circ$ below the x – y plane (Figure S11).³⁹

Confirming the lowering of symmetry from the idealized case, the ¹⁴N ENDOR simulations resolve strong coupling of an axially symmetric ¹⁴N ligand with a hyperfine tensor of $|A(^{14}N)| = [29, 30, 47]$ MHz and quadrupole coupling of $e^2qQ/h = 2.4$ MHz, $\eta_Q = 0.67$. Importantly, the hyperfine and quadrupole tensors must be rotated by Euler angles $[\alpha, \beta, \gamma] = [14, 16, 0]^\circ$ with respect to the g -tensor to obtain the best match to the experimental data; attempts to obtain a valid simulation without including this rotation gave significantly worse fits to the data (Figure S8).

Encouraged by these experimental findings, we then employed computational methods to further probe the electronic implications of the inequivalence of the two methyl groups. Indeed, the DFT-optimized structure of square pyramidal complex **3** reveals two inequivalent methyl groups, with an in-plane (ip) methyl group in the equatorial plane and a Ni–C_{ip} distance of 1.9584 Å, while the out-of-plane (op) methyl group lies 21° below the equatorial plane and a Ni–C_{op} distance of 1.9735 Å (Figure 1 and Figure S21). In addition, the calculated frontier molecular orbitals (FMOs) exhibit significant contributions from the methyl ligand orbitals, underscoring the covalent nature of the Ni-alkyl interactions.

The singly occupied molecular orbital (SOMO) is mainly metal-centered, with a 68.9% Ni d_z^2 atomic orbital contribution and a 74% spin localization on the Ni center, supporting the metal radical nature of this complex (Figure 3 and Table S2).

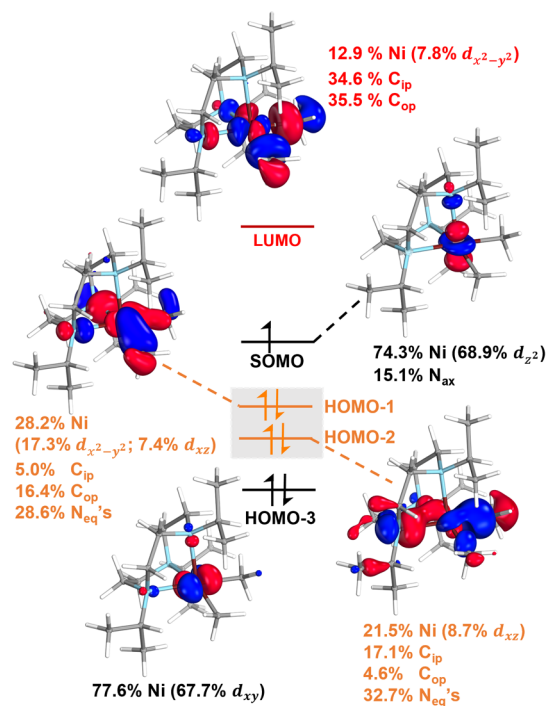


Figure 3. DFT-calculated frontier molecular orbitals (FMOs) of complex **3**, obtained at the B3LYP/def2-TZVPP/SMD//B3LYP/def2-TZVPP/SV(P)/SMD level of theory. The FMOs are depicted with a 0.05 isovalue, along with Löwdin atomic orbital contributions of >5%.

The substantial contribution of the axial N atom to the SOMO is predicted to result in large hyperfine coupling values that are in good agreement with those observed in the ENDOR spectra (Table S3), validating the accuracy of the calculated electronic structure. By comparison, the LUMO is mainly ligand-centered, with $\sim 35\%$ contributions from each C atom of the two methyl groups and only a 12.9% contribution from the Ni center (Figure 3), suggesting that this system exhibits appreciable inverted ligand field character.^{15,16,20} Interestingly, the HOMO–1 and HOMO–2 orbitals reveal highly covalent Ni-ligand bonding interactions: HOMO–1 has 28.2% Ni character along with a 16.4% contribution from C_{op} and 5.0% from C_{ip}, while HOMO–2 has 21.5% Ni character along with a 17.1% contribution from C_{ip} and 4.6% from C_{op}, and both HOMO–1 and HOMO–2 have a combined contribution of $\sim 30\%$ from the equatorial N atoms of the ⁱPr₃TACN ligand (Figure 3). By inspection, HOMO–1 is the likely bonding MO that corresponds to the antibonding LUMO, based on the contributing Ni $d_{x^2-y^2}$ orbital and the C_{op}/C_{ip} AOs, while HOMO–2 seems to be almost equally distributed over the Ni center and the C_{ip} atom, suggesting a strong radical character for the Ni–C_{ip} bond.

To probe in more detail the covalent nature of the Ni-methyl interactions and the inequivalence of the two methyl ligands, we employed the IBO and EOS analyses developed by Knizia et al.^{34–36} and Salvador et al.,^{37,38} respectively, and employed recently by Klein et al. for high-valent organo-

metallic Ni complexes.¹⁴ IBO analysis of the Ni–ligand interactions reveals that the three Ni–N bonding interactions with the ⁱPr₃tacn ligand are dative in nature, with the calculated partial charges mainly residing on the N atoms (Figure 4A–

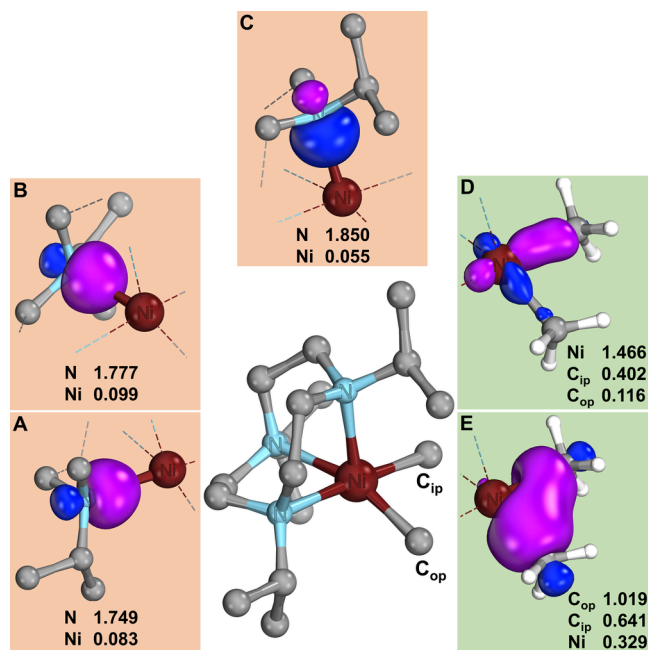


Figure 4. IBO depictions of the five Ni–ligand bonding IBOs. Numbers in parentheses indicate the partial charge distribution of a given IBO at the B3LYP/def2-TZVPP/SMD//B3LYP/def2-TZVP/SV(P)/SMD level of theory. The IBOs are depicted using IboView at an isosurface value of 70%.

C). By comparison, one Ni–C IBO is mainly localized on the Ni center (1.466 partial charge) and the C_{ip} atom (0.402 partial charge, Figure 4D), and resembling an inverted ligand field interaction, while the other Ni–C IBO is best described as a dative interaction that is delocalized over both C_{ip} and C_{op} atoms of the two methyl groups (Figure 4E), resembling a 2-electron, 3-center bond. Overall, this IBO analysis strongly suggests that the two methyl groups are electronically inequivalent. The Ni–C_{ip} bonding interaction is highly covalent, with direct implications for the formal oxidation

state assignment for the Ni center. Indeed, EOS analysis of complex 3 reveals that the Ni center is best described as having an oxidation state of +II (fragment 1, Table S5), the in-plane methyl group is assigned an oxidation state of 0 (Fragment 2), thus having a strong radical character, while the out-of-plane methyl group is assigned an oxidation state of –I (fragment 3), thus acting as an X type ligand. The ⁱPr₃tacn ligand is assigned an oxidation state of 0 and, therefore, is redox innocent. Overall, the differential electronic description of the two methyl ligands is expected to directly impact the reductive elimination reactivity of Ni–dialkyl complex 3 (see below).

Further spectroscopic investigation of the electronic structure of complex 3 was performed using three-pulse ESEEM spectroscopy on ²H-labeled samples (Figure 5 and Figures S12–S19). Along with contributions from weakly coupled nitrogens, likely due to the two equatorial N ligands, time-domain traces from the Ni^{III}(CD₃)₂ sample show significant modulations from coupling to ²H nuclei (Figure S12). While the spectra are complicated due to multiplicative interactions between chemically inequivalent ²H and ¹⁴N nuclei, global simulations of the τ - and field-dependent ESEEM spectra have been used to constrain approximate hyperfine coupling values for each set of methyl deuterons (Figures S13–S15). One methyl group has $|A(^2\text{H}_1)| = [1.5, -1.2, 0.9]$ MHz ($a_{\text{iso}} = 0.4$ MHz; $T = 0.8$ MHz; $\eta_A = 0.4$), with the unique axis along g_2 and a quadrupolar coupling $e^2qQ/h = 0.3$ MHz and $\eta_Q = 1$. The second methyl group has a hyperfine tensor $|A(^2\text{H}_2)| = [-1, 2, 0.4]$ MHz ($a_{\text{iso}} = 0.47$ MHz; $T = 0.77$ MHz; $\eta_A = 0.9$), with a fully rhombic hyperfine tensor and large quadrupolar contribution $e^2qQ/h = 1$ MHz and $\eta_Q = 0.6$ (Figure S16). Alternative simulations using either identical hyperfine parameters for both methyl groups or interchanging the quadrupolar values do not reproduce the major spectral features, which is particularly apparent on the single-crystal-like edges of the absorption envelope (Figures S17–S19).

HYSCORE spectra of complex 3 resolve overlapping ESEEM signals and provide a better measure of the anisotropy of hyperfine coupling. Although both ¹H and ²H HYSCORE spectra show signals centered at ν_{H} across different field positions, the ridge features in the Ni^{III}(CH₃)₂ sample show a much greater extension away from the diagonal and deeper modulation signals. In addition, deep modulations contributing to cross peaks centered at the deuterium Larmor frequency

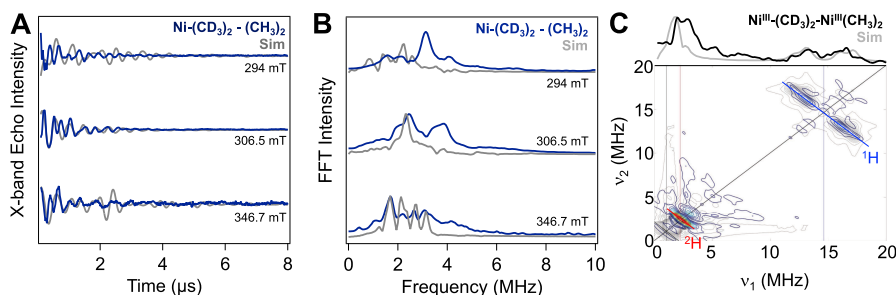


Figure 5. X-band pulsed EPR hyperfine characterization of Ni^{III}(CD₃)₂. (A) Three-pulse ESEEM time-domain decay traces of Ni^{III}(CD₃)₂–Ni^{III}(CH₃)₂ (blue) collected across the absorption envelope with simulations overlaid (gray) ($T = 15$ K; $\nu_{\mu\text{w}} = 9.77$ GHz). (B) Three-pulse ESEEM spectra generated by fast Fourier transform (FFT) of time-domain data and simulations shown in (A). (C) Ni^{III}(CD₃)₂–Ni^{III}(CH₃)₂ subtracted HYSCORE spectrum at 343 mT with the simulated spectrum overlaid ($T = 15$ K; $\nu_{\mu\text{w}} = 9.70$ GHz). Frequency domain skyline plots are shown above the HYSCORE spectra. Larmor frequencies for the following nuclei are shown as vertical lines with the cross-peaks indicated on the graph: ¹H (blue), ²H (red), and ¹⁴N (black). Simulation parameters: $|A(^2\text{H}_1)| = [1.5, -1.2, 0.9]$ MHz; $|Q(^2\text{H}_1)| = [-0.25, 0.1, 0.15]$ MHz; $|A(^2\text{H}_2)| = [-1, 2, 0.4]$ MHz; $|Q(^2\text{H}_2)| = [-0.1-0.4, 0.5]$ MHz. ¹H simulation parameters were obtained by scaling the ²H hyperfine tensor values by the 6.51:1 ratio of the respective nuclear Larmor frequencies.

ridges are seen in the $\text{Ni}^{\text{III}}(\text{CD}_3)_2$ samples. Simulations of the HYSORE spectra (Figure S20) recapitulate key peaks arising from the two distinct $-\text{CD}_3$ groups and reproduce the position and curvature of the ^1H peaks, reflecting the anisotropy of the ^1H hyperfine coupling. Collectively, the ESEEM and HYSORE data reveal that the two methyl groups coordinated to the nickel center are not equal from an electronic structure standpoint.

A second simulation approach was attempted, in which the quadrupolar values were constrained to $e^2qQ/h = 0.2$ MHz and $\eta_Q = 0.1$, with the unique axes rotated 90° for each methyl group and in line with previously reported values.^{40–45} With these constraints, satisfactory fits to the ESEEM traces were obtained, but there was poor agreement with the breadth and shape of the ^1H ridges in the HYSORE spectra (Figure S19), and unphysical distances between the nickel center and deuterium nuclei were extrapolated.

Similar to our previous characterization of an $S = 1/2$ $\text{Ni}-\text{CH}_3$ species in an azurin protein,¹⁶ the point-dipole approximation was utilized to approximate a distance between the nickel and the two sets of methyl deuterium atoms in the $\text{Ni}^{\text{III}}(\text{CD}_3)_2$ sample. Under the assumption of fully localized spin on the nickel center, which provides an upper bound on the separation between spin centers, average $\text{Ni}-\text{D}$ distances of 2.49 and 2.52 Å were calculated using the point-dipole approximation (Figure 6). These experimentally resolved

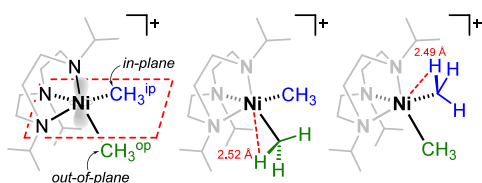


Figure 6. $\text{Ni}\cdots\text{H}(\text{CH}_3)$ distances estimated from pulsed EPR experiments, which support the inequivalent nature of the two methyl groups in $[(\text{Pr}_3\text{TACN})\text{Ni}(\text{CH}_3)_2]^+$ complex 3.

distances are in good agreement with the asymmetry predicted by the DFT-optimized structures, which predict an 0.03 Å longer average $\text{Ni}-\text{D}$ distances for the out-of-plane methyl group vs the in-plane methyl group, with average distances of 2.54 and 2.57 Å, respectively.¹⁶ Moreover, the observed slight flattening of the in-plane methyl group is likely due to the increased radical character of this methyl group, as suggested by the IBO and EOS analysis.

Having obtained strong experimental evidence and computational support that the two methyl groups in complex 3 are geometrically and electronically inequivalent, with the in-plane methyl group having a more pronounced radical character (along with the Ni center being in the + II oxidation state), we set out to probe the reductive elimination step to generate the C–C coupled product from this catalytically relevant intermediate.²⁶ The calculated reaction coordinate does indeed predict a favorable reductive elimination step with an accessible transition state (Figure S23), while EOS analysis of both the transition state structure and the Ni product reveals an oxidation state of +I for the Ni center (Table S7), which suggests a concerted, intramolecular homolytic alkyl–alkyl coupling step. Interestingly, such a homolytic step resembles the recently proposed $\text{S}_{\text{H}2}$ cross-coupling mechanism for alkyl–alkyl bond formation at high-valent metal centers.^{46,47}

We then extended the computational analysis to mixed Ni-dialkyl systems with one methyl group and another alkyl group (ethyl, isopropyl, or *tert*-butyl), which should more closely resemble the catalytic intermediates formed during an alkyl–alkyl cross-coupling reaction. Interestingly, the DFT-calculated geometries and electronic structures of complex 3 and its methyl/alkyl analogs reveal an increasing spin density on the larger alkyl group that is in the in-plane position, along with an increase in the $\text{Ni}-\text{C}_{\text{ip}}$ bond length (Figure 7). By comparison,

Complex	$[\text{LNiMe}_2]^+$	$[\text{LNiMeEt}]^+$	$[\text{LNiMePr}]^+$	$[\text{LNiMe}^t\text{Bu}]^+$
$\text{Ni}-\text{C}_{\text{alkyl}}$ (in-plane)	1.9584	1.9636	2.0507	2.0646
$\text{Ni}-\text{C}_{\text{methyl}}$ (out-of-plane)	1.9735	1.9576	1.9580	1.9458
Spin Density on alkyl (ip)	-0.098	-0.105	-0.136	-0.176
Spin Density on methyl (op)	-0.079	-0.057	-0.067	-0.048

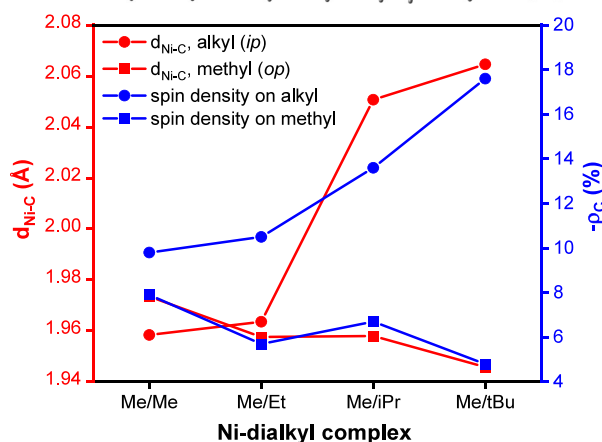
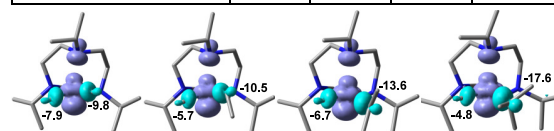


Figure 7. DFT-calculated $\text{Ni}-\text{C}_{\text{alkyl}}$ distances (Å) for the varied alkyl groups, calculated at the B3LYP/def2TZVPP/SMD level of theory. Löwdin spin densities (%) on the differentiated alkyl groups of complex 3 and its methyl/alkyl analogs, obtained from the EOS analysis. Spin density plots are shown at an isovalue of 0.005. The bottom plot is a graphical representation of the variation of the tabulated $\text{Ni}-\text{C}$ bond distances and the alkyl group spin densities for complex 3 and its methyl/alkyl analogs.

the spin density on the out-of-plane methyl group and the corresponding $\text{Ni}-\text{C}_{\text{op}}$ bond lengths decrease slightly. Moreover, the EOS analysis of these methyl/alkyl analogs of 3 also reveals that the in-plane alkyl groups exhibit radical character (Table S6), in line with the increased spin density found in these groups. Overall, these mixed Ni-methyl/alkyl complexes support the recently proposed ability of Ni systems to preferentially bind smaller, less stable primary alkyl radicals,⁴⁶ while the larger, secondary, or tertiary alkyl groups should be more weakly bound to Ni and exhibit radical character. Thus, we propose that the alkyl–alkyl reductive elimination steps at formally high-valent Ni centers could be viewed as a concerted $\text{S}_{\text{H}2}$ -type reductive elimination, in which one of the alkyl groups has an appreciable radical character. Such a mechanism would be the intramolecular variant of the intermolecular $\text{S}_{\text{H}2}$ process proposed by MacMillan et al. in the recently developed alkyl–alkyl coupling processes promoted by high-valent metal centers.^{46,47}

CONCLUSIONS

In summary, herein, we report a comprehensive pulsed EPR experimental study and computational investigation into a catalytically relevant high-valent organometallic Ni-dialkyl complex in which the bulky tridentate ligand renders the two alkyl groups geometrically and electronically inequivalent. The inequivalence of the two alkyl groups has significant implications for the oxidation state assignment of this formal organometallic Ni^{III} complex, in which one alkyl group exhibits significant radical character, and the metal center can be better described as a Ni^{II} center. Moreover, we have extended the computational analysis to high-valent Ni-dialkyl species containing two different alkyl groups to provide evidence for the preferred localization of the radical character on the secondary and tertiary alkyl groups versus primary alkyl groups. This provides a selectivity rule for the radical sorting process needed to promote efficient alkyl–alkyl cross-coupling reactions. Overall, this study offers valuable insights into the intricate interplay between the ligand geometry, the highly covalent metal–alkyl interactions, and the formal oxidation state assignment of organometallic Ni-dialkyl species, and ultimately the key factors that promote efficient alkyl–alkyl cross-coupling reactions through an S_H2-type mechanism.

ASSOCIATED CONTENT

Supporting Information

The Supporting Information is available free of charge at <https://pubs.acs.org/doi/10.1021/jacs.4c14104>.

Computational details, computational data, and additional experimental details for the pulsed EPR studies (PDF)

AUTHOR INFORMATION

Corresponding Authors

Hannah S. Shafaat – Department of Chemistry and Biochemistry and Ohio State Biochemistry Program, The Ohio State University, Columbus, Ohio 43210, United States; Present Address: Department of Chemistry and Biochemistry, University of California, Los Angeles, 607 Charles E. Young Drive E, Los Angeles, CA 90095, United States (H.S.S.); orcid.org/0000-0003-0793-4650; Email: shafaat@ucla.edu

Liviu M. Mirica – Department of Chemistry, University of Illinois at Urbana–Champaign, Urbana, Illinois 61801, United States; orcid.org/0000-0003-0584-9508; Email: mirica@illinois.edu

Authors

Alina Yerbulekova – Department of Chemistry and Biochemistry and Ohio State Biochemistry Program, The Ohio State University, Columbus, Ohio 43210, United States

Yusuff Moshood – Department of Chemistry, University of Illinois at Urbana–Champaign, Urbana, Illinois 61801, United States

Leonel Griego – Department of Chemistry, University of Illinois at Urbana–Champaign, Urbana, Illinois 61801, United States

Complete contact information is available at:

<https://pubs.acs.org/doi/10.1021/jacs.4c14104>

Author Contributions

[#]A.Y. and Y.M. contributed equally.

Notes

The authors declare no competing financial interest.

ACKNOWLEDGMENTS

We thank the National Science Foundation (CHE-2155160 to L.M.M.) and the Department of Energy (DE-SC0023137 and DE-SC0024869 to H.S.S. and A.Y.) for their support. We also thank the UIUC's School of Chemical Sciences High-Performance Computing Center for processor time, and Adam Jenkins and Justin Malme for their assistance with computational studies.

REFERENCES

- (1) Campeau, L.-C.; Hazari, N. Cross-Coupling and Related Reactions: Connecting Past Success to the Development of New Reactions for the Future. *Organometallics* **2019**, *38*, 3–35.
- (2) Diccianini, J. B.; Diao, T. Mechanisms of Nickel-Catalyzed Cross-Coupling Reactions. *Trends Chem.* **2019**, *1*, 830–844.
- (3) Choi, J.; Fu, G. C. Transition metal-catalyzed alkyl-alkyl bond formation: Another dimension in cross-coupling chemistry. *Science* **2017**, *356*, No. eaaf7230.
- (4) Tasker, S. Z.; Standley, E. A.; Jamison, T. F. Recent advances in homogeneous nickel catalysis. *Nature* **2014**, *509*, 299–309.
- (5) Hu, X. Nickel-catalyzed cross coupling of non-activated alkyl halides: a mechanistic perspective. *Chem. Sci.* **2011**, *2*, 1867–1886.
- (6) Jones, G. D.; McFarland, C.; Anderson, T. J.; Vivic, D. A. Analysis of key steps in the catalytic cross-coupling of alkyl electrophiles under Negishi-like conditions. *Chem. Commun.* **2005**, 4211–4213.
- (7) Jones, G. D.; Martin, J. L.; McFarland, C.; Allen, O. R.; Hall, R. E.; Haley, A. D.; Brandon, R. J.; Kononova, T.; Desrochers, P. J.; Pulay, P.; Vivic, D. A. Ligand redox effects in the synthesis, electronic structure, and reactivity of an alkyl-alkyl cross-coupling catalyst. *J. Am. Chem. Soc.* **2006**, *128*, 13175–13183.
- (8) Vechorkin, O.; Hu, X. Nickel-Catalyzed Cross-Coupling of Non-activated and Functionalized Alkyl Halides with Alkyl Grignard Reagents. *Angew. Chem., Int. Ed.* **2009**, *48*, 2937–2940.
- (9) Bour, J. R.; Camasso, N. M.; Meucci, E. A.; Kampf, J. W.; Canty, A. J.; Sanford, M. S. Carbon–Carbon Bond-Forming Reductive Elimination from Isolated Nickel(III) Complexes. *J. Am. Chem. Soc.* **2016**, *138*, 16105–16111.
- (10) Roberts, C. C.; Camasso, N. M.; Bowes, E. G.; Sanford, M. S. Impact of Oxidation State on Reactivity and Selectivity Differences between Nickel(III) and Nickel(IV) Alkyl Complexes. *Angew. Chem., Int. Ed.* **2019**, *58*, 9104–9108.
- (11) Bour, J. R.; Ferguson, D. M.; McClain, E. J.; Kampf, J. W.; Sanford, M. S. Connecting Organometallic Ni(III) and Ni(IV): Reactions of Carbon-Centered Radicals with High-Valent Organonickel Complexes. *J. Am. Chem. Soc.* **2019**, *141*, 8914–8920.
- (12) Hoffmann, R.; Alvarez, S.; Mealli, C.; Falceto, A.; Cahill, T. J., III; Zeng, T.; Manca, G. From Widely Accepted Concepts in Coordination Chemistry to Inverted Ligand Fields. *Chem. Rev.* **2016**, *116*, 8173–8192.
- (13) Bour, J. R.; Camasso, N. M.; Sanford, M. S. Oxidation of Ni(II) to Ni(IV) with Aryl Electrophiles Enables Ni-Mediated Aryl-CF₃ Coupling. *J. Am. Chem. Soc.* **2015**, *137*, 8034–8037.
- (14) Steen, J. S.; Knizia, G.; Klein, J. E. M. N. σ -Noninnocence: Masked Phenyl-Cation Transfer at Formal NiIV. *Angew. Chem., Int. Ed.* **2019**, *58*, 13133–13139.
- (15) Wilson, C. V.; Kim, D.; Sharma, A.; Hooper, R. X.; Poli, R.; Hoffman, B. M.; Holland, P. L. Cobalt–Carbon Bonding in a Salen-Supported Cobalt(IV) Alkyl Complex Postulated in Oxidative MHAT Catalysis. *J. Am. Chem. Soc.* **2022**, *144*, 10361–10367.
- (16) Kisgeropoulos, E. C.; Manesis, A. C.; Shafaat, H. S. Ligand Field Inversion as a Mechanism to Gate Bioorganometallic Reactivity: Investigating a Biochemical Model of Acetyl CoA Synthase Using Spectroscopy and Computation. *J. Am. Chem. Soc.* **2021**, *143*, 849–867.

- (17) Walroth, R. C.; Lukens, J. T.; MacMillan, S. N.; Finkelstein, K. D.; Lancaster, K. M. Spectroscopic Evidence for a 3d10 Ground State Electronic Configuration and Ligand Field Inversion in [Cu(CF3)4]−1. *J. Am. Chem. Soc.* **2016**, *138*, 1922–1931.
- (18) DiMucci, I. M.; Lukens, J. T.; Chatterjee, S.; Carsch, K. M.; Titus, C. J.; Lee, S. J.; Nordlund, D.; Betley, T. A.; MacMillan, S. N.; Lancaster, K. M. The Myth of d8 Copper(III). *J. Am. Chem. Soc.* **2019**, *141*, 18508–18520.
- (19) Lukens, J. T.; DiMucci, I. M.; Kurogi, T.; Mindiola, D. J.; Lancaster, K. M. Scrutinizing metal–ligand covalency and redox non-innocence via nitrogen K-edge X-ray absorption spectroscopy. *Chem. Sci.* **2019**, *10*, 5044–5055.
- (20) DiMucci, I. M.; Titus, C. J.; Nordlund, D.; Bour, J. R.; Chong, E.; Grigas, D. P.; Hu, C.-H.; Kosobokov, M. D.; Martin, C. D.; Mirica, L. M.; Nebra, N.; Vivic, D. A.; Yorks, L. L.; Yruegas, S.; MacMillan, S. N.; Shearer, J.; Lancaster, K. M. Scrutinizing formally NiIV centers through the lenses of core spectroscopy, molecular orbital theory, and valence bond theory. *Chem. Sci.* **2023**, *14*, 6915–6929.
- (21) Zheng, B.; Tang, F. Z.; Luo, J.; Schultz, J. W.; Rath, N. P.; Mirica, L. M. Organometallic Nickel(III) Complexes Relevant to Cross-Coupling and Carbon-Heteroatom Bond Formation Reactions. *J. Am. Chem. Soc.* **2014**, *136*, 6499–6504.
- (22) Tang, F. Z.; Rath, N. P.; Mirica, L. M. Stable bis-(trifluoromethyl)nickel(III) complexes. *Chem. Commun.* **2015**, *51*, 3113–3116.
- (23) Schultz, J. W.; Fuchigami, K.; Zheng, B.; Rath, N. P.; Mirica, L. M. Isolated Organometallic Nickel(III) and Nickel(IV) Complexes Relevant to Carbon-Carbon Bond Formation Reactions. *J. Am. Chem. Soc.* **2016**, *138*, 12928–12934.
- (24) Watson, M. B.; Rath, N. P.; Mirica, L. M. Oxidative C–C Bond Formation Reactivity of Organometallic Ni(II), Ni(III), and Ni(IV) Complexes. *J. Am. Chem. Soc.* **2017**, *139*, 35–38.
- (25) Smith, S. M.; Rath, N. P.; Mirica, L. M. Axial Donor Effects on Oxidatively Induced Ethane Formation from Nickel–Dimethyl Complexes. *Organometallics* **2019**, *38*, 3602–3609.
- (26) Griego, L.; Chae, J. B.; Mirica, L. M. A bulky 1,4,7-triazacyclononane and acetonitrile, a Goldilocks system for probing the role of Ni^{III} and Ni^I centers in cross-coupling catalysis. *Chem.* **2024**, *10*, 867–881.
- (27) Reilly, J.; Charron, G.; Rivière, E.; Guillot, R.; Barra, A.; Serrano, M. D.; van Slageren, J.; Mallah, T. Large magnetic anisotropy in pentacoordinate Ni–II complexes. *Chem.—Eur. J.* **2008**, *14*, 1169–1177.
- (28) Griego, L.; Woods, T. J.; Mirica, L. M. A five-coordinate Ni(I) complex supported by 1,4,7-triisopropyl-1,4,7-triazacyclononane. *Chem. Commun.* **2022**, *58*, 7360–7363.
- (29) Neese, F. The ORCA program system. *WIREs Comput. Mol. Sci.* **2012**, *2*, 73–78.
- (30) Becke, A. D. Density-functional thermochemistry. III. The role of exact exchange. *J. Chem. Phys.* **1993**, *98*, 5648–5652.
- (31) Lee, C. T.; Yang, W. T.; Parr, R. G. Development of the Colle-Salvetti Correlation-Energy Formula Into a Functional of the Electron-Density. *Phys. Rev. B—Cond. Matter* **1988**, *37*, 785–789.
- (32) Weigend, F.; Ahlrichs, R. Balanced basis sets of split valence, triple zeta valence and quadruple zeta valence quality for H to Rn: Design and assessment of accuracy. *Phys. Chem. Chem. Phys.* **2005**, *7*, 3297–3305.
- (33) Neese, F.; Wennmohs, F.; Becker, U.; Riplinger, C. The ORCA quantum chemistry program package. *J. Chem. Phys.* **2020**, *152*, 224108.
- (34) Knizia, G. Intrinsic Atomic Orbitals: An Unbiased Bridge between Quantum Theory and Chemical Concepts. *J. Chem. Theory Comput.* **2013**, *9*, 4834–4843.
- (35) Vidossich, P.; Lledós, A. The use of localised orbitals for the bonding and mechanistic analysis of organometallic compounds. *Dalton Trans.* **2014**, *43*, 11145–11151.
- (36) Knizia, G.; Klein, J. E. M. N. Electron Flow in Reaction Mechanisms—Revealed from First Principles. *Angew. Chem., Int. Ed.* **2015**, *54*, 5518–5522.
- (37) Ramos-Cordoba, E.; Postils, V.; Salvador, P. Oxidation States from Wave Function Analysis. *J. Chem. Theory Comput.* **2015**, *11*, 1501–1508.
- (38) Gimferrer, M.; Aldossary, A.; Salvador, P.; Head-Gordon, M. Oxidation State Localized Orbitals: A Method for Assigning Oxidation States Using Optimally Fragment-Localized Orbitals and a Fragment Orbital Localization Index. *J. Chem. Theory Comput.* **2022**, *18*, 309–322.
- (39) Rao, G.; Altman, A. B.; Brown, A. C.; Tao, L.; Stich, T. A.; Arnold, J.; Britt, R. D. Metal Bonding with 3d and 6d Orbitals: An EPR and ENDOR Spectroscopic Investigation of Ti3+–Al and Th3+–Al Heterobimetallic Complexes. *Inorg. Chem.* **2019**, *58*, 7978–7988.
- (40) Lucken, E. A. C. *Nuclear Quadrupole Coupling Constants*. Academic Press: London, 1969.
- (41) Brecht, M.; van Gastel, M.; Bührke, T.; Friedrich, B.; Lubitz, W. Direct Detection of a Hydrogen Ligand in the [NiFe] Center of the Regulatory H2-Sensing Hydrogenase from *Ralstonia eutropha* in Its Reduced State by HYSCORE and ENDOR Spectroscopy. *J. Am. Chem. Soc.* **2003**, *125*, 13075–13083.
- (42) Yang, N.; Reiher, M.; Wang, M.; Harmer, J.; Duin, E. C. Formation of a nickel-methyl species in methyl-coenzyme M reductase, an enzyme catalyzing methane formation. *J. Am. Chem. Soc.* **2007**, *129*, 11028–11029.
- (43) Harmer, J.; Finazzo, C.; Piskorski, R.; Ebner, S.; Duin, E. C.; Goenrich, M.; Thauer, R. K.; Reiher, M.; Schweiger, A.; Hinderberger, D.; Jaun, B. A Nickel Hydride Complex in the Active Site of Methyl-Coenzyme M Reductase: Implications for the Catalytic Cycle. *J. Am. Chem. Soc.* **2008**, *130*, 10907–10920.
- (44) Marchiori, D. A.; Oyala, P. H.; Debus, R. J.; Stich, T. A.; Britt, R. D. Structural Effects of Ammonia Binding to the Mn4CaO5 Cluster of Photosystem II. *J. Phys. Chem. B* **2018**, *122*, 1588–1599.
- (45) Arnett, C. H.; Bogacz, I.; Chatterjee, R.; Yano, J.; Oyala, P. H.; Agapie, T. Mixed-Valent Diiron μ -Carbyne, μ -Hydride Complexes: Implications for Nitrogenase. *J. Am. Chem. Soc.* **2020**, *142*, 18795–18813.
- (46) Mao, E.; MacMillan, D. W. C. Late-Stage C(sp³)–H Methylation of Drug Molecules. *J. Am. Chem. Soc.* **2023**, *145*, 2787–2793.
- (47) Liu, W.; Lavagnino, M. N.; Gould, C. A.; Alcázar, J.; MacMillan, D. W. C. A biomimetic SH₂ cross-coupling mechanism for quaternary sp³-carbon formation. *Science* **2021**, *374*, 1258–1263.